Earth and Space Science

RESEARCH ARTICLE
10.1029/2018EA000502

Special Section:
The Arctic: An AGU Joint Special Collection

Improved Arctic Ocean Bathymetry Derived From DTU17 Gravity Model

Adili Abulaitijiang[1], Ole Baltazar Andersen[1], and David Sandwell[2]

[1]DTU Space, Technical University of Denmark, Lyngby, Denmark, [2]Scripps Institute of Oceanography, University of California, San Diego, La Jolla, CA, USA

Key Points:
- The first ever Arctic bathymetry inverted from DTU17 gravity anomalies is presented
- Good agreement between the ship soundings and inverted bathymetry is achieved

Supporting Information:
- Supporting Information S1

Correspondence to:
A. Abulaitijiang,
adili@space.dtu.dk

Citation:
Abulaitijiang, A., Andersen, O. B., & Sandwell, D. (2019). Improved Arctic Ocean bathymetry derived from DTU17 gravity model. *Earth and Space Science*, *6*, 1336–1347. https://doi.org/10.1029/2018EA000502

Received 13 OCT 2018
Accepted 20 JUN 2019
Accepted article online 8 JUL 2019
Published online 3 AUG 2019

Abstract The existing bathymetry map of the Arctic is a compilation of ship soundings and digitized contours. Due to the presence of all-year sea ice, costly operations and political restrictions, dense and full coverage of the Arctic is not possible, leaving huge gaps between the existing surveys. In this paper, we make use of the existing Arctic bathymetry IBCAOv3 and invert Arctic bathymetry from the recent altimetric gravity model DTU17, whose accuracy is improved significantly with revised data processing strategy. The long and short wavelength components are preserved from IBCAOv3. The band-pass-filtering function proposed by Smith and Sandwell (1994, https://doi.org/10.1029/94JB00988) is adapted for the Arctic by reducing the cutoff wavelength. The predicted bathymetry is within 100 m on 85.8% of the grid nodes, when compared to the IBCAOv3. The consistency of the prediction is validated with two independent profiles from Healy cruises conducted in 2016 over the Chukchi Cap. A questionable valley in the IBCAOv3 is detected with gravity and at this spot, bathymetry predicted from gravity is consistent with independent multibeam soundings. The gravity-inverted bathymetry could be combined with ship soundings for the next generation of Arctic bathymetry map.

1. Introduction

The sea floor topography plays an important role in understanding geological tectonic evolution, geophysical and oceanographic studies, for example, ice-ocean interaction, ocean circulation, and tidal modeling (Cancet et al., 2018). Several global bathymetry models of the oceans are developed, namely, the General Bathymetric Chart of the Oceans (GEBCO, latest version GEBCO_2019; Weatherall et al., 2015), Refined Topography data set (RTopo, latest version RTopo-2; Schaffer et al., 2016), and the new global topography SRTM30_PLUS (Becker et al., 2009). The global models are combinations of different data sources dedicated for Arctic, Antarctic, and general oceans. RTopo-2 includes new regional data sets released recently, for example, the Greenland continental shelf and fjords (Arndt et al., 2015; Bamber et al., 2013) and the edges of Antarctic ice shelf (Le Brocq et al., 2010). The latest bed topography of Greenland (BedMachine, Version 3) is developed by integrating new bathymetry data from different sources (Morlighem et al., 2017). All the models partially or fully integrate the International Bathymetric Chart of the Arctic Ocean (IBCAO) to achieve complete coverage in the Arctic regions.

However, the Arctic Ocean bathymetry is not well surveyed due to the presence of sea ice and harsh climate in the polar region. There have been campaigns to map the sea floor topography through ship sounding, but it only covers the very small fraction of the entire Arctic, and meanwhile, it is very costly to operate. The most recent release of IBCAO (Version 3.0, IBCAOv3; Jakobsson et al., 2012) is obtained by interpolating the sparse ship sounding data into a loosely constrained regular grid. Where the grid cells are unconstrained by ship soundings, depths are obtained by interpolation. Digitized bathymetric contours are extensively used for gridding and to fill the data gaps. The Arctic bathymetry and the source of ship sounding data used in the IBCAOv3 production are shown in Figure 1.

Most part of the Arctic Ocean, such as the East Siberian Sea, Chukchi Sea, Kara Sea, and Barents Sea, are very shallow, with average depth ranging from 50 to 230 m. These continental shelves are relatively flat and have steep topographic variations at the margins to the major basins (e.g., Canada basin). A physiographic classification of Arctic Ocean seafloor and general description of geological features are presented by Jakobsson et al. (2003). The Chukchi Cap extends from the north of Alaska toward the Arctic Ocean and has been the region of interest in extending the definition of the continental shelf seaward following Article 76 of United Nations Convention of the Law of the Sea (Gardner et al., 2006). The thickness of

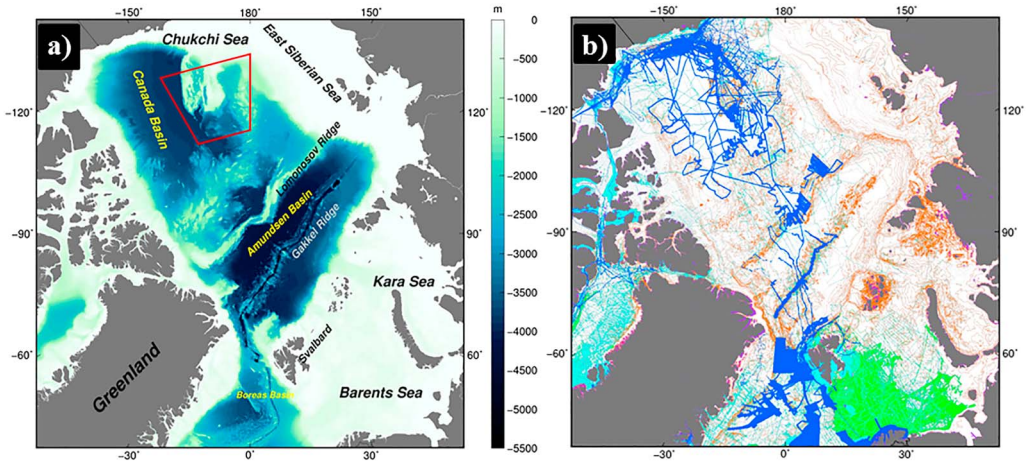

Figure 1. Maps showing (a) the IBCAOv3 bathymetry; the area bounded by the red box is Chukchi Cap (plateau); (b) the source of the ship sounding data used for IBCAOv3 production (Jakobsson et al., 2012); purple color indicates data from land digital elevation model, blue color indicates data from multibeam data, cyan color indicates single-beam data, green indicates data from Olex (www.olex.no), and orange indicates depth contours from digitized charts.

sediments (Døssing et al., 2014; Laske & Masters, 1997) in the deep Amundsen basin is approximately 2 km, while it is up to 11 km in the Canada basin (May & Grantz, 1990). The sedimentary basins appear nearly flat on the bathymetry maps.

The sea surface gravity and sea floor topography relationship is described by McKenzie and Bowin (1976) and Parker (1973). On a limited bandwidth, the linear correlation between band-pass-filtered gravity and bathymetry is estimated by statistical Pearson's correlation coefficient and the gravity-to-topography ratio (or scaling factor) can be determined by robust linear regression.

Smith and Sandwell (1994) developed the algorithm to predict the bathymetry from gravity in the 1990s. The global bathymetry models predicted from altimetric gravity so far goes up to latitude 81°N; however, the bathymetry beyond that latitude has not been predicted from gravity due to the less accurate marine gravity at high latitudes. Gravity inversion has been applied for the large-scale subcrust geometry estimation and sediment thickness mapping, in combination with seismic soundings (Alvey et al., 2008; Engen et al., 2006; Glebovsky et al., 2013). However, the accuracy of the existing bathymetry (IBCAOv3) is still uncertain at the high latitudes.

In this paper, we present the first result of Arctic bathymetry map inverted from the most recent altimetric gravity model DTU17. The spatial correlation between band-pass-filtered gravity and bathymetry is made to estimate the scaling parameter between gravity and bathymetry. The results from Smith and Sandwell (1994) algorithm and its modified version are presented and validated with the input IBCAOv3. Predicted bathymetry is validated with two multibeam ship sounding surveys that are released after the production of IBCAOv3 in 2012.

2. Data and Algorithm

2.1. Bathymetry Data

The existing bathymetry map IBCAOv3 is a compilation of multibeam, single-beam, Olex seabed mapping (www.olex.no) system and digital contour maps with a grid spacing of 500 m (Polar Stereographic projection, with true latitude at 75°N) and reveals detailed features on the sea floor. The bathymetry grid nodes are well constrained when the sounding data are available. However, the areas with no soundings are interpolated to fill the gaps (Jakobsson et al., 2012). The IBCAOv3 serves as the base for the input bathymetry grid.

2.2. Gravity Data

The accuracy of long wavelength (greater than 100 km) gravity field in the Arctic is slightly poorer than that in the midlatitudes. The long wavelength signal in the DTU17 gravity model (Andersen & Knudsen, 2019) is from Earth Gravitational Model 2008 (EGM2008; Pavlis et al., 2012), in which the primary data source in the

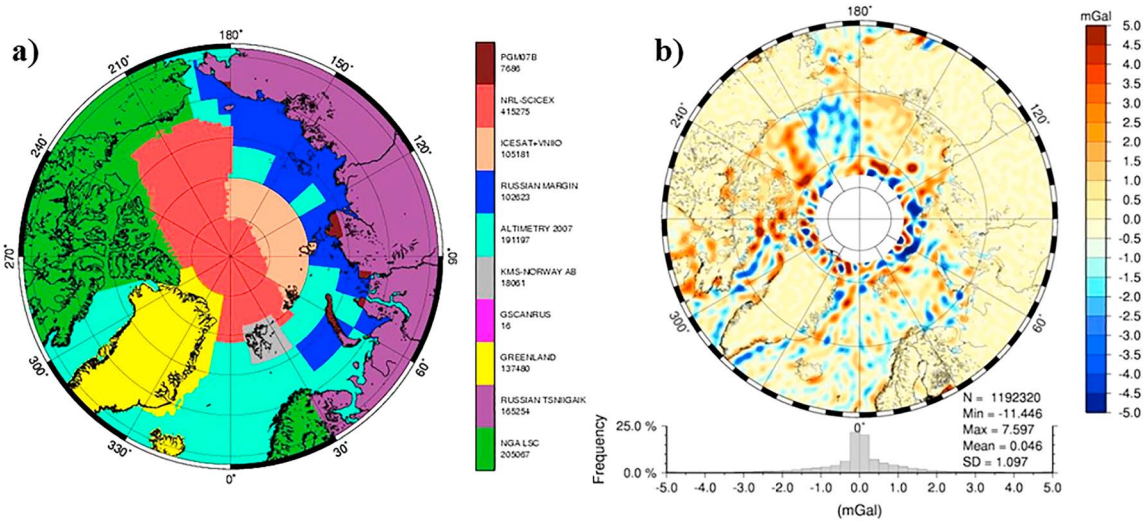

Figure 2. (a) The source of gravity data information in the ArcGP project (Kenyon & Forsberg, 2008); (b) The difference of ArcGP gravity field (EGM2008) and combined satellite-only gravity model GOCO05S (Mayer-Gürr et al., 2015) up to degree and order 200 (corresponding half-wavelength 100 km). Courtesy of Simon Holmes.

Arctic is from the Arctic Gravity Project (ArcGP; Kenyon & Forsberg, 2008), see Figure 2. As much as 5 mGal difference is observed on the long wavelength gravity field, when the ArcGP gravity anomalies are compared to GOCO05S satellite-only gravity model (Mayer-Gürr et al., 2015). The differences are partly attributed to the patched gravity data from multiple sources in the ArcGP. Moreover, the differences at higher latitudes (>80°N) are significant (Pail et al., 2018). If not filtered properly, these could be translated into bathymetry prediction error.

The altimetric gravity model developed at DTU Space included the 25 years of satellite altimetry data over the ocean. Between 70°N and 81.5°N, the ERS-1/2, EnviSat, 7 years of CryoSat-2 altimetry data, and 1 year of SARAL/AltiKa data from geodetic phase is used; between 81.5°N and 88°N, only CryoSat-2 data is used; the remaining polar gap is filled by the ArcGP gravity compilations. The latest version DTU17 marine gravity model (1-arcmin grid spacing) is released with a main improvement in the Arctic where the accuracy is increased from 9.82 (for EGM2008) to 3.78 mGal when compared to the LOMGRAV-09 aerogeophysical survey north of Greenland between 82°N and 90°N (see Figure S1 and S2 in the supporting information). The huge improvement in the Arctic motivated us to predict the bathymetry from gravity. The geographic grid of DTU17 is coregistered to the IBCAOv3 bathymetry grid using Polar Stereographic projection.

2.3. Land Mask

In addition to the input bathymetry and gravity grids, we need a land mask so to constrain the correlation analysis only to the points over the ocean. The Global Self-consistent, Hierarchical, High-resolution Geography database (Wessel & Smith, 1996) coastlines assembled in the Generic Mapping Tool (Wessel & Smith, 1991; Wessel et al., 2013) are imported and coregistered with the bathymetry grid using Polar Stereographic projection.

2.4. Algorithm

In the Polar Stereographic coordinate system, the coordinates of a grid node are given by easting and northing. For simplicity, the coordinates are denoted by a symbol x in the following. The predicted bathymetry $H_p(x)$ can be written as the sum of the long wavelength component of the input bathymetry $B_{long}(x)$, inverted topography from band-pass-filtered gravity $G_{BP}(x)$ and remaining short-wavelength components from the high-pass filter of the input bathymetry $B_{\text{short}}(x)$, as below

$$H_p(x) = B_{\text{long}}(x) + S(x) \cdot G_{BP}(x) + B_{\text{short}}(x), \tag{1}$$

where $S(x)$ is the scaling factor used to convert gravity to topography, with unit m/mGal.

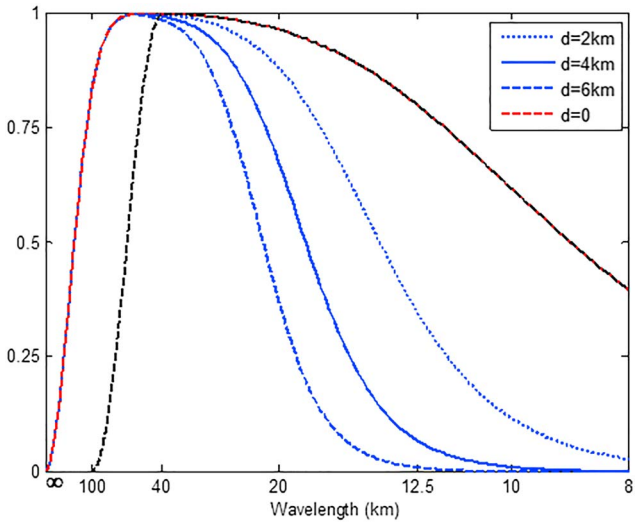

Figure 3. The S&S filter $W(k) = W_1(k)W_2(k)$ without exponential term at different depth d is shown in blue color. Modified S&S filter $W_m(k) = W_c(k)W_2(k)$ with $d = 0$, is shown by the black dashed curve. The horizontal axis is converted from wave number k to wavelength in kilometer.

The details of algorithm used for the development of Arctic bathymetry can be referred to the paper from Smith and Sandwell (1994). The assumed correlation in the wavelength between the downward continued gravity and bathymetry is between 15 and 160 km. In the Arctic, there might be errors on the long wavelength components in the gravity. Therefore, a proper band-pass-filtering function has to be designed to obtain the band-pass-filtered gravity and bathymetry.

The band-pass-filtering function proposed by Smith and Sandwell (1994) is referred as Smith&Sandwell (S&S) filter in the following sections. The general form is

$$W(k) = W_1(k) \cdot W_2(k) \cdot \exp[2\pi k d], \tag{2}$$

where $W_1(k)$ is a high-pass Gaussian filter; $W_2(k)$ is a low-pass filter, the exponential term is the downward continuation operator, in which d is the depth in kilometers, and k is the wave number with unit per kilometer; the forms for $W_1(k)$ and $W_2(k)$ are

$$W_1(k) = 1 - \exp\left[-2(\pi k s)^2\right], \tag{3}$$

$$W_2(k) = \left\{1 + Ak^4 \exp[4\pi k d]\right\}^{-1}. \tag{4}$$

The s in $W_1(k)$ is the Gaussian parameter ($s = 30$ km) with assumed crust thickness of 7 km; the $W_1 = 0.5$ when $k^{-1} = 160$ km; the A parameter in $W_2(k)$ is a constant chosen by the spectral coherence (between bathymetry and gravity) analysis, here we used $A = 6{,}233$ km^4; $W_2(k)$ is a function of depth, and in the deeper ocean depths (e.g., $d = 6$ km), the gravity signal is suppressed by this filter at "longer" wavelengths, compared to that of shallow sea floor (e.g., $d = 2$ km), see Figure 3.

As described in the previous section, the long wavelength error in the Arctic has to be suppressed to avoid the prediction error in the bathymetry. A new filter is designed to accommodate the S&S filter for the Arctic. Here it is referred as modified S&S filter $W_m(k)$. A cosine-taper filter $W_c(k)$ replaces the $W_1(k)$ high-pass filter to cut off the wavelength greater than 100 km and pass the wavelength shorter than 40 km.

$$W_c(k) = 0.5 \times \left[1 + \cos\left(\pi \bullet \frac{k - k_p}{k_c - k_p}\right)\right], \tag{5}$$

where the k_c is the cutoff wave number (1/100 km^{-1}) and k_p is the high-pass wave number (1/40 km^{-1}). Thus, the $W_c = 0.5$ when $k^{-1} = 57$ km. Then, the modified S&S filter is given by

$$W_m(k) = W_c(k) \cdot W_2(k) \cdot \exp[2\pi k d]. \tag{6}$$

The combination of $W_1(k)$ and $W_2(k)$ yields a band-pass-filtering function as shown in Figure 3. All the operations are conducted in the wave number domain. Since the grids are uniformly sampled in the polar stereographic projection (500-m grid spacing), we apply forward Fourier transform to the entire grid.

The long wavelength component of the input bathymetry $B_{\text{long}}(x)$ is obtained by low-pass filtering as below

$$B_{\text{long}}(k) = B(k)[1 - W_*(k)] \tag{7}$$

where $B(k)$ is a Fourier transform of the input bathymetry grid (IBCAOv3), $W_*(k)$ is either $W_1(k)$ in equation (3) or $W_c(k)$ in equation (4).

The bathymetry grid is filtered with $W(k)$ or $W_m(k)$ to obtain the band-pass-filtered bathymetry $B_{\text{BP}}(k)$, where the depth term $d = 0$, which corresponds to the red or black dashed curve in Figure 3.

After applying the filtering function, an inverse Fourier transform is needed to achieve the band-pass-filtered version of the gravity $G_{\text{BP}}(x)$ and bathymetry $B_{\text{BP}}(x)$ grids, and the gravity-to-topography scaling

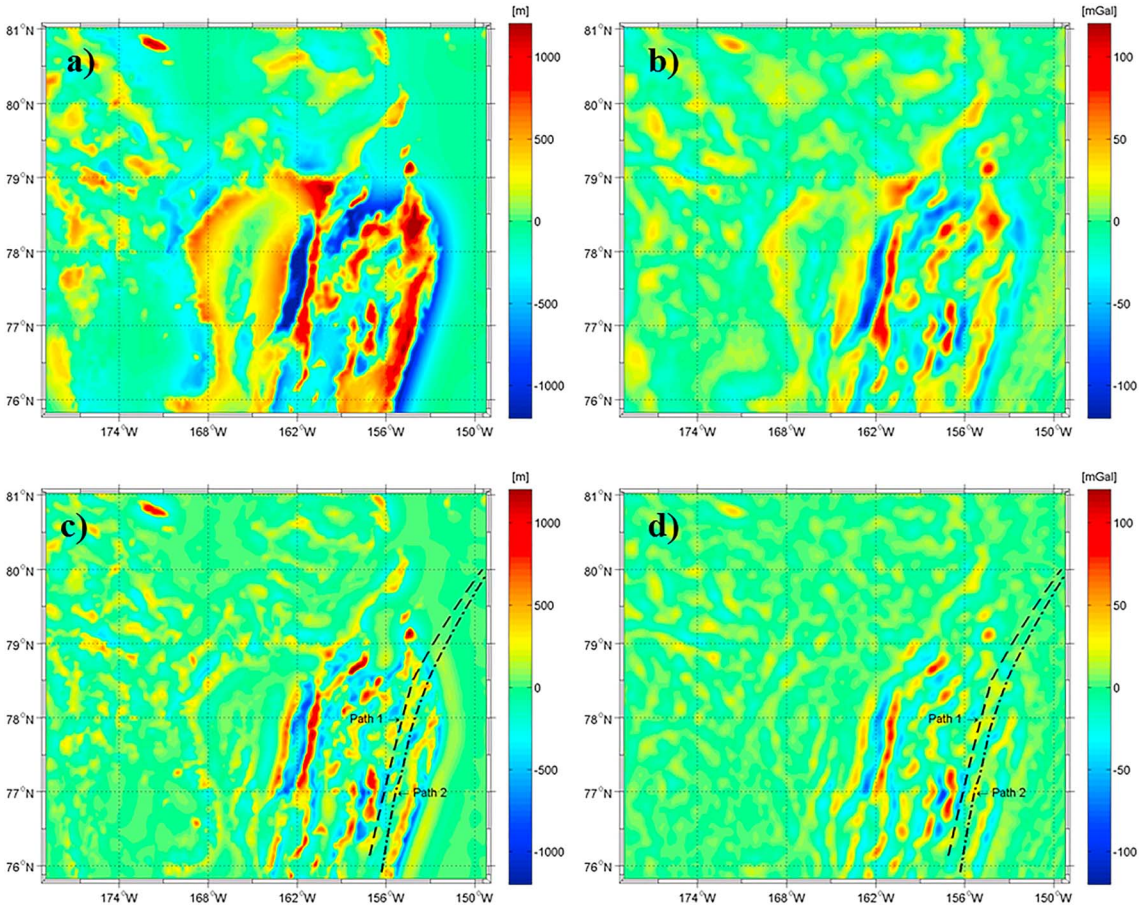

Figure 4. Band-pass-filtered bathymetry (a) and gravity (b) when using $W(k)$ from Smith and Sandwell (1994); Band-pass-filtered bathymetry (c) and gravity (d) when using modified S&S filter $W_m(k)$ proposed in this paper. Two northbound Healy cruises from HE1603 crossing the Chukchi Cap are shown by the dashed curve, which will be used for profile analysis later.

parameter $S(x)$ is estimated from these two data sets. In Figure 4, the band-pass-filtered bathymetry and gravity of the area bounded by the red box in Figure 1a are shown. The remaining long wavelength features are evident when using the $W(k)$ filter (in which $W_1 = 0.5$ when $k^{-1} = 160$ km).

Following Smith and Sandwell (1994), we make use of the Median Absolute Deviation (MAD) of the $G_{\mathrm{BP}}(x)$ and $B_{\mathrm{BP}}(x)$ values g_{mad} and h_{mad} for the estimation of $S(x)$, see equation (8). The Smith and Sandwell approach is denoted as "slope estimator" in the following. The grid spacing of $S(x)$ is 30 km, and gravity and bathymetry pairs within the 30-km radius block are used for one scaling factor estimation. Meanwhile, only grid nodes over the oceans (through a land-ocean mask) are used for this estimation.

$$S(x) = \mathrm{sign}[\rho]\frac{h_{\mathrm{mad}}}{g_{\mathrm{mad}}}, \tag{8}$$

where ρ is the linear correlation coefficient estimated from data pairs. The correlation can be any value between -1 and 1. The sign of the correlation coefficient is assigned to the scaling factor $S(x)$ as indicated in equation (8).

The magnitude of $S(x)$ is subject to the small changes in g_{mad} and h_{mad}. Alternative to the slope estimator (equation (8)), we can use RANdom SAmple Consensus (RANSAC) algorithm (Fischler & Bolles, 1981) as a robust estimator of the scaling parameter $S(x)$. An example of the RANSAC estimates along with the slope estimators (equation (8)) are shown in Figure 5. The scaling parameter $S(x)$ is estimated at the center of the 30-km radius block. One scaling factor (slope of the line fitted to the scattered pairs in Figures 5e and 5f) is estimated for a pair of band-pass-filtered gravity and bathymetry block. In contrast, the linear least squares

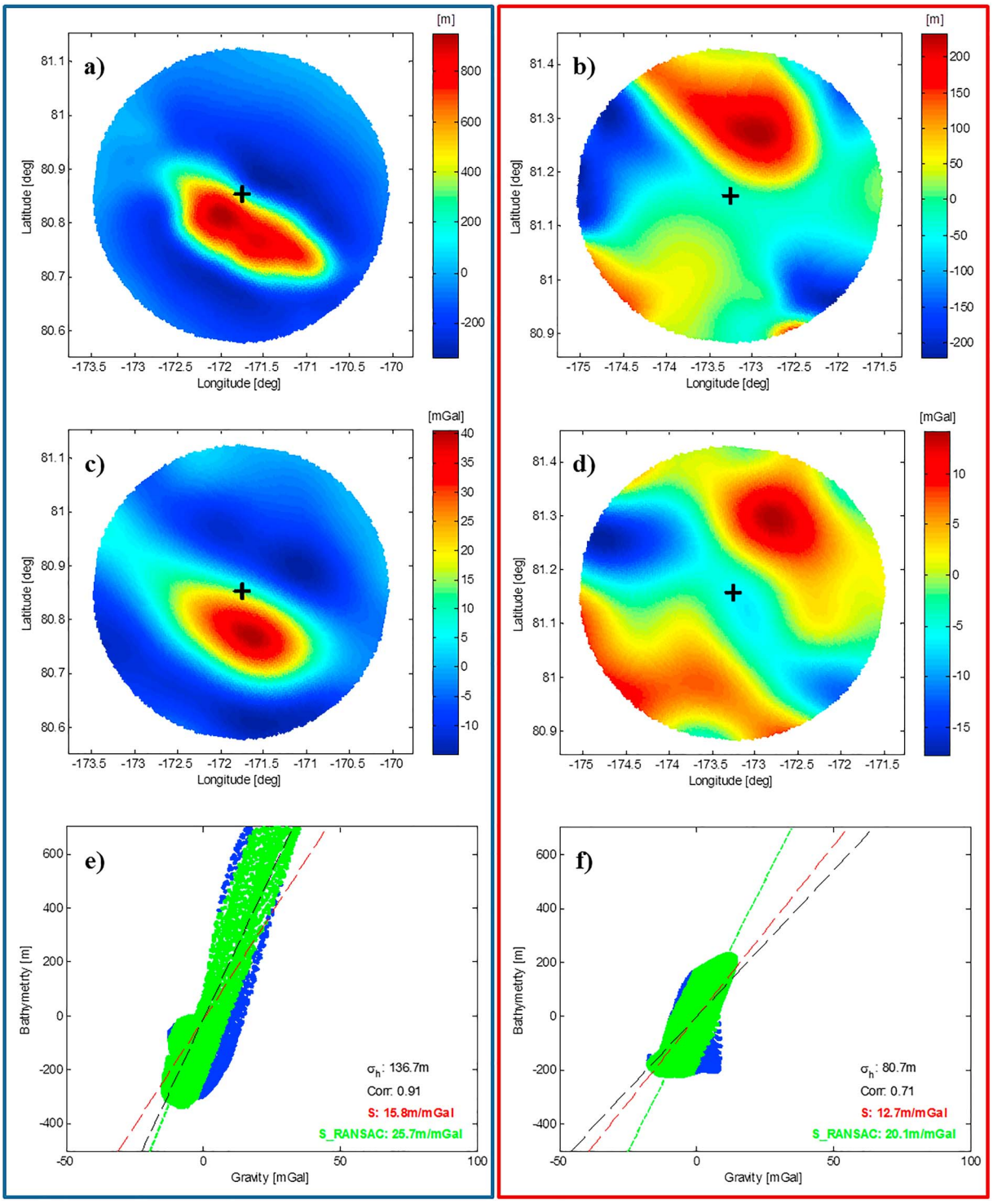

Figure 5. Illustrations of scaling factor estimations at two different locations. Blue frame on the left refers to a spot over a seamount, while the red frame on the right refers to a region with moderate topographic variations. Top two rows: band-pass-filtered bathymetry (a and b) and gravity (c and d) in a 30-km radius cap. Thick black + marker shows the center of the cap and it is the location of local scaling factor $S(x)$. Bottom row: local scaling factor $S(x)$ (e and f; slope of the lines) estimated using different algorithms. Red line for the slope estimator (equation (8)), green for the RANSAC estimator and black for the least squares fitting. The scattered points for band-pass-filtered bathymetry and gravity are marked in blue, while the green RANSAC inliers are superimposed on them. RANSAC = RANdom SAmple Consensus.

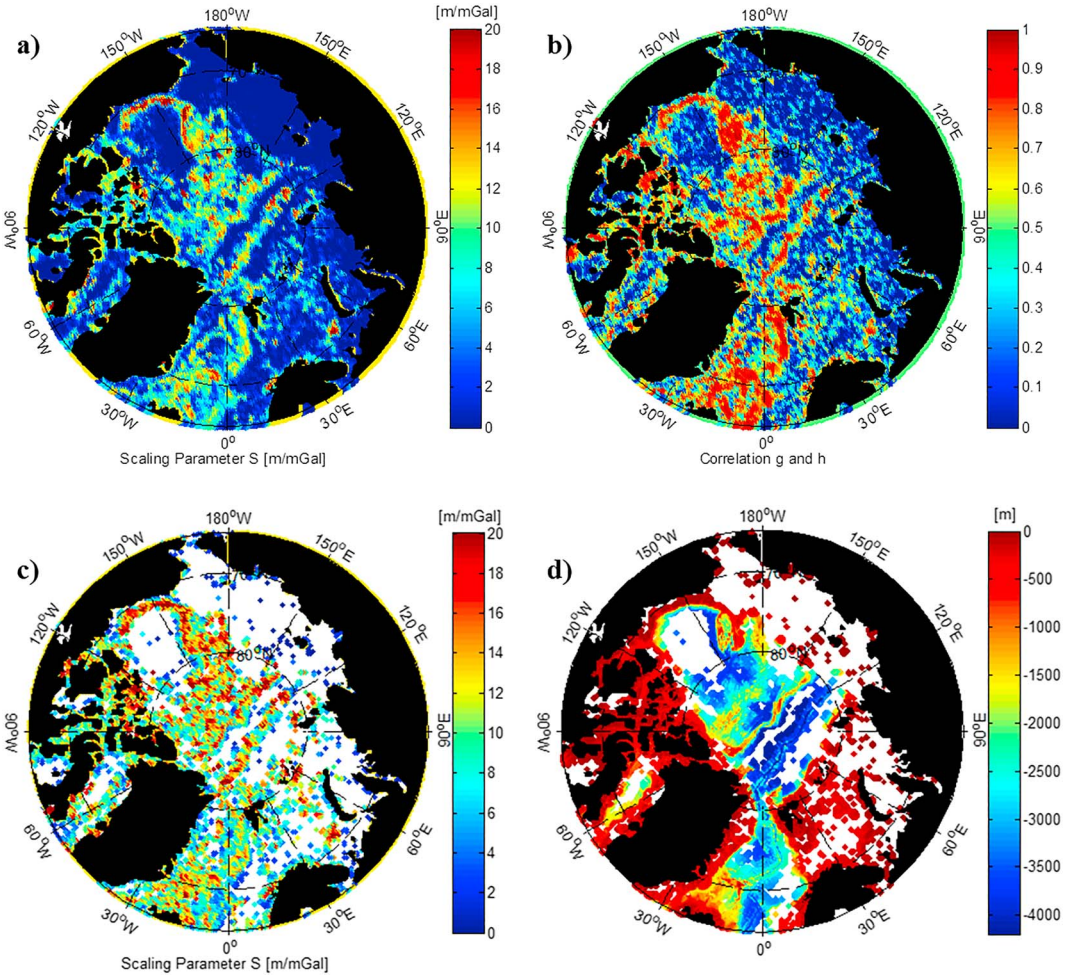

Figure 6. (a) Scaling factor $S(x)$ estimated on 30-km spacing grid nodes, (b) correlation coefficients between band-pass-filtered gravity and bathymetry on a grid spacing of 30 km in the Arctic, when the modified S&S filter $W_m(k)$ is used. (c) Scaling parameters where correlation between topography and gravity is higher than 0.5. (d) Predicted bathymetry on grid nodes where significant correlations are observed.

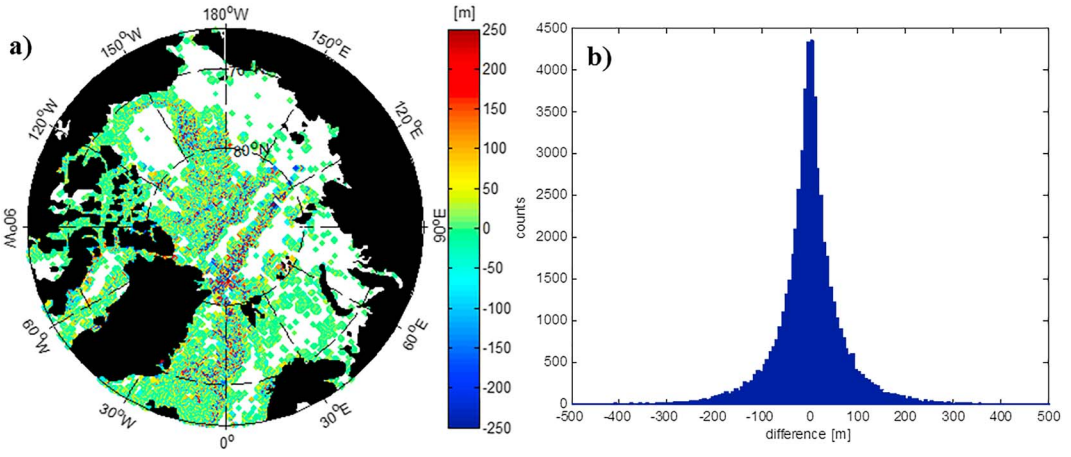

Figure 7. (a) The difference of predicted bathymetry and IBCAOv3, when the modified S&S filter $W_m(k)$ is used. (b) Histogram of differences between predicted bathymetry and IBCAOv3.

Table 1
The Difference of Predicted Bathymetry $H_p(x)$ and IBCAOv3 Using Different High-Pass Filtering Functions, $|\Delta h|$ Implies Absolute Difference and Showing the Percentage of Grid Nodes That Are Smaller Than 100 m

High-pass filter	$\|\Delta h\| < 100$	Mean	Std.	Min	Max
$W_1(k)$	64.8%	7.7	143.7	−1531.8	1,862.2
$W_c(k)$	85.8%	−0.5	81.5	−782.9	1,129.7

Note. Unit: m.

fitting (LSF, shown in black dashed line in Figure 5, bottom panel) is also tested. The estimated slope from LSF is close to RANSAC, but it could deviate dramatically from the RANSAC estimates when the data pairs are widely scattered, see Figure 5f.

The advantage of RANSAC algorithm is that it will try to search for the most "inliers" in the scattered data, and the "outliers" will not be considered for the slope estimation. As shown in Figure 5, the RANSAC algorithm fits to the general extent of the scattered data. A difference of 10 m/mGal in the scaling factor gives a difference of 400 m in the predicted bathymetry, which is significant over the seamounts..

3. Results

The scaling parameter and spatial correlation on a grid spacing of 30 km is shown in Figures 6a and 6b. On most part of the shallow continental shelf in the Arctic, both the correlation and scaling factor is low. In such parts, we simply set $S(x) = 0$, and keep the original bathymetry grid values.

Moderate correlation and scaling factor $S(x)$ are obtained over the Chukchi Cap, along the Gakkel Ridge, Lomonosov Ridge, and the north Atlantic Boreas basin. The topography is inverted from gravity in these regions.

We used a correlation threshold of 0.5 to filter out the low correlation nodes in the $S(x)$ grid (Figure 6c). The ocean ridges and continental shelf margins are visible after screening out nodes with low correlation. Grid nodes at the sedimentary Canada basin and Amundsen basin, along with shallow continental shelves around the Russian coast, are filtered out. To achieve the predicted heights, the 30-km spacing $S(x)$ grid is interpolated and coregistered with the band-pass-filtered gravity grid $G_{\mathrm{BP}}(x)$. This is achieved by General Mapping Tool *surface* module. Then the converted bathymetry can be computed. At the very final step, the fine scale features of the bathymetry $B_{\mathrm{short}}(x)$ (derived from $[1 - W_2(k)]$ high-pass filter) should be added back, to have the predicted bathymetry $H_p(x)$, see Figure 6d.

Subsequently, we can compare our prediction resulting from modified S&S filter $W_m(k)$ with the initial input bathymetry grids (IBCAOv3) on the same grid nodes. The differences are shown in Figure 7. The mean difference is −0.5 m and the standard deviation (std.) of the differences is 81.5 m. On 85.8% of the grid nodes, the absolute differences are less than 100 m. This indicates that the bathymetry inverted from gravity has good agreement with the existing bathymetry of the Arctic in general. However, very large differences are observed at Gakklel ridge, which is located more than 3,500 m below sea level. From the source identification grid in Figure 1b, we can observe that there are dense multibeam surveys right along the ridge axis, which maps the detailed features of local seafloor. The cause of the differences can be attributed to the

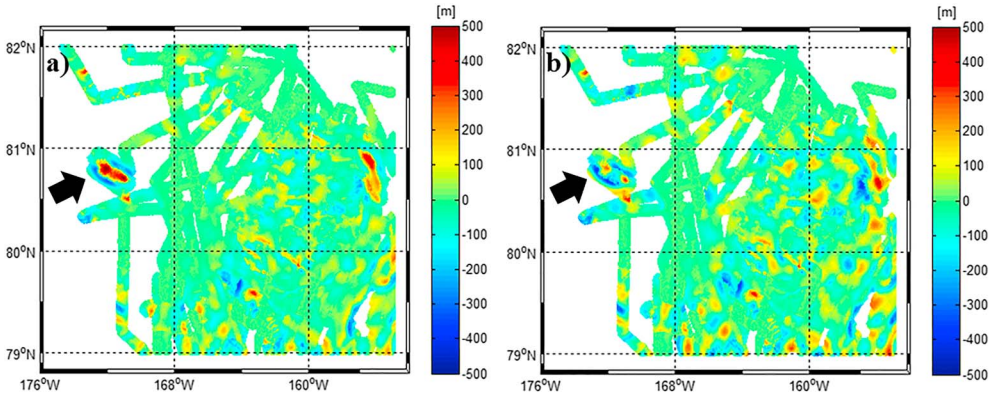

Figure 8. The difference of compiled ECS (multibeam) bathymetry data and predicted bathymetry resulting from different scaling factor estimation algorithms on the north of Chukchi Cap. (a) Scaling factor estimated from Smith and Sandwell approach (equation (8)), (b) scaling factor estimated from RANSAC algorithm. Gravity and bathymetry were filtered with modified S&S filter $W_m(k)$. In total, 268,105 multibeam samples (500-m spacing) are used in this comparison.

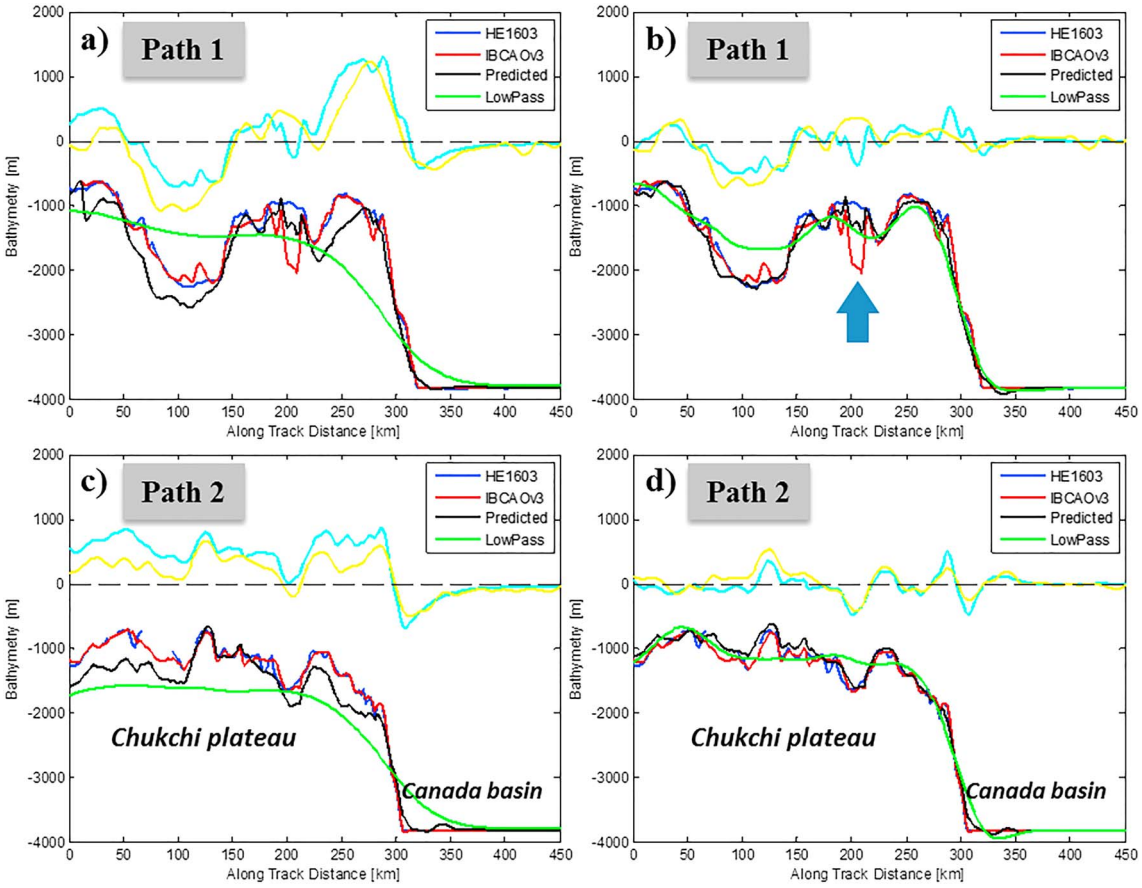

Figure 9. The along-track profiles of Healy cruise path 1 (a, b) and path 2 (c, d). Subfigures (a) and (c) refer to the results from the Smith and Sandwell (1994) filter. Subfigures (b) and (d) refer to the results from the modified filter $W_m(k)$. Blue curve for the HE1603, red curve for the IBCAOv3, black curve for the predicted bathymetry in this study, green curve for the low-pass filtered bathymetry $B_{\text{long}}(x)$, cyan for band-pass-filtered bathymetry, and yellow for the band-pass-filtered gravity which is scaled by scaling factor $S(x)$.

downward continued gravity to deep sea floor of ~4 km, which only resolve larger than 18-km features. Thus, in some wavelengths we do not predict bathymetry. Such large differences were also observed in the southern ocean studies from Smith and Sandwell (1994).

In addition, the comparison with bathymetry predicted using the S&S filter $W(k)$ and its modified version $W_m(k)$ (the main difference is $W_1(k)$ and $W_c(k)$ for the high-pass filtering) is given in Table 1. The predicted bathymetry from the S&S filter gives relatively large differences compared to the modified filter proposed in this study.

4. Validation

The bathymetric sounding surveys can be accessed through NOAA National Centers for Environmental Information (NCEI, formerly NGDC) Bathymetry Data Viewer map services. There are limited amounts of ship soundings conducted after the release of IBCAOv3. Most of the ship sounding multibeam data are collected as part of Extended Continental Shelf (ECS) project and led by scientists from the University of New Hampshire and U.S. Geological Survey. The target region of ECS project is mainly around the Chukchi Cap and only few cruise tracks operated toward the North Pole (Mayer et al., 2016; Mayer & Armstrong, 2012). The differences of ECS compilation and IBCAOv3 give a mean of −11.4 m with a std. of 48.0 m. It is worth to mention that most of the cruises that operated before 2012 have already been incorporated to IBCAOv3. Therefore, only several latest cruises are relatively independent for external validation, for instance, HE1202 (Mayer & Armstrong, 2012) and HE1603 (Mayer et al., 2016).

Table 2
The Statistics of the Differences From Profile Analysis

Profiles	Differece	Mean	Std.	Min	Max
Path 1	HE1603 − $H_p(x)_1$	160.4	195.7	−134.1	731.2
	HE1603 − IBCAOv3	33.9	181.6	−295.8	1012.8
	$H_p(x)_1$ − IBCAOv3	−126.0	243.3	−636.0	677.3
Path 2	HE1603 − $H_p(x)_2$	114.6	182.8	−246.3	531.6
	HE1603 − IBCAOv3	2.3	54.1	−225.8	175.2
	$H_p(x)_2$ − IBCAOv3	−126.3	184.6	−514.6	233.8

Note. Bathymetry prediction results from S&S filter $W(k)$. $H_p(x)_1$ and $H_p(x)_2$ are profiles for paths 1 and 2, respectively. Refer to the profiles in Figures 9a and 9c. Unit: m.

A closer view on the difference of compiled ECS ship sounding compilations (from 2003 to 2016) and our bathymetry estimate to the north of Chukchi Cap is shown in Figure 8. Positive differences indicate that the bathymetry predicted from gravity is deeper than ship soundings, and thus implies that the actual heights of seamount are underestimated (by as much as 400 m). Negative differences indicate that the predicted bathymetry is shallower than ship soundings, ~100 m (mainly over the deep relatively flat basins). In Figure 8, ECS bathymetry compilations are compared to bathymetry resulting from different scaling factor estimation algorithms described in section 2.4. The results from scaling factor $S(x)$ estimated using slope estimator (equation (8)) appear smoother than the results obtained from RANSAC. RANSAC estimator performs better than the slope estimator over a seamount marked by the black arrow. In fact, this is exactly the spot where we demonstrated the scaling factor estimation in Figure 5a. On average, scaling factor estimated from RANSAC is 6.6 m/mGal higher than that estimated from slope estimator. Therefore, more fluctuations are visible on the results obtained from RANSAC (Figure 8b). The mean difference between ECS bathymetry data and bathymetry resulting from slope estimator (refer to Figure 8a) is −11.6 m, with a std. of 71.7 m. It is −13.0 ± 81.0 m for the differences referring to RANSAC in Figure 8b. One should be careful when employing RANSAC algorithm to entire region. We recommended using RANSAC estimator over rugged topography with large variations.

In the following, two profiles taken from Healy cruise multibeam sounding surveys conducted in 2016 (HE1603) are analyzed. Locations of the two profiles are shown in Figure 4c. From south to north, the two paths cross the margin of Chukchi Cap (plateau) at the along-track distance ~300 km as shown in Figure 9. The profiles referring to S&S filter are shown in Figures 9a and 9c, where predicted bathymetry (black curve) deviates as much as 200 m from IBCAOv3 and HE1603 profiles over Chukchi plateau. Such deviations are evident on both profiles of paths 1 and 2. The profiles referring to the modified S&S filter are shown in Figures 9b and 9d. Compared to the results from S&S filter, predicted bathymetry shows good agreement with HE1603 profiles as well as IBCAOv3. No dramatic deviations are observed on both profiles. At the along-track distance ~200 km in Figure 9b, the blue arrow indicates a spot where IBCAOv3 is problematic. At this spot, an ~1,000-m-deep valley was mapped in existing IBCAOv3. However, the ship soundings from HE1603 comply with the bathymetry inverted from gravity at this spot.

The statistics of the profile analysis along the two paths (see locations in Figure 4c) are shown in Tables 2 and 3. When using the S&S filter, both the mean and std. of the differences are large compared to the results from the modified S&S filter. On path 1, standard deviation of differences between HE1603 and predicted bathymetry is 119.5 m, which is 39% improvement to the bathymetry using S&S filter on this profile. Moreover, the mean difference on path 1 is reduced from 160.4 to 50.8 m. Smaller mean difference indicates consistency between predicted bathymetry and HE1603. On path 2, the mean difference is only −36.9 m with a std. of 77.6 m as shown in Table 3. Compared to a std. of 182.8 m from bathymetry using S&S filter, 57% improvement is obtained from bathymetry using modified S&S filter. In particular, the standard deviation of differences between HE1603 and IBCAOv3 on path 1 is 181.6 m. Differences between HE1603 and predicted bathymetry using modified S&S filter yield a std. of 119.5 m, which is 33% improvement to the existing IBCAOv3.

Table 3
The Statistics of the Differences From Profile Analysis

Profiles	Difference	Mean	Std.	Min	Max
Path 1	HE1603 − $H_p(x)_1$	50.8	119.5	−211.9	413.8
	HE1603 − IBCAOv3	33.9	181.6	−295.8	1012.8
	$H_p(x)_1$ − IBCAOv3	−16.9	161.8	−438.6	694.0
Path 2	HE1603 − $H_p(x)_2$	−36.9	77.6	−237.4	202.6
	HE1603 − IBCAOv3	2.3	54.1	−225.8	175.2
	$H_p(x)_2$ − IBCAOv3	51.2	89.2	−233.4	285.5

Note. Bathymetry prediction results from the modified S&S filter $W_m(k)$. $H_p(x)_1$ and $H_p(x)_2$ are profiles for paths 1 and 2, respectively. Refer to the profiles in Figures 9b and 9d. Unit: m.

The profile analysis and validation with independent ship soundings suggest that the modified S&S filter is successful in predicting Arctic Ocean bathymetry from gravity anomalies.

5. Summary

The accuracy of marine gravity in the Arctic Ocean was found to be significantly improved in the DTU17 marine gravity model. The improvement in gravity motivated us to predict bathymetry from gravity anomalies in the Arctic Ocean. In this paper, we presented the first ever Arctic bathymetry predicted from marine gravity. The Smith&Sandwell filter has to

be adjusted for the Arctic to diminish the long wavelength error in the gravity at the high latitudes. Modified version of Smith&Sandwell filter is proposed to overcome the potential long wavelength problem in the Arctic Ocean.

The prediction is only done on grid nodes where the bathymetry and gravity variations are significant. Significant correlation is observed over the Chukchi Cap, along the Gakkel Ridge, Lomonosov Ridge, and the north Atlantic Boreas basins. On most of the shallow water regions and the sedimentary basins, such as Canada basin and Amundsen basin, low or negative correlation between gravity and topography is observed. In such regions, bathymetry is not predicted from gravity.

The scaling factor is an important parameter in predicting bathymetry from gravity. The Smith and Sandwell approach (slope estimator) tends to underestimate the actual seafloor topography. RANSAC algorithm suggested in this study was found to be effective over the rugged topography (e.g., seamounts) and predicted bathymetry is closer to the accurate depth measurements from ship soundings.

Good agreement between the predicted bathymetry and input bathymetry IBCAOv3 is achieved when applying modified Smith&Sandwell filter. Overall, the mean difference is −0.5 m, with a std. of 81.5 m. The validation with compiled ECS bathymetry over the north of Chukchi Cap, and two Healy cruise profiles shows good consistency between the predicted bathymetry and ship soundings. In addition, a questionable valley is detected in the IBCAOv3 through the profile analysis.

The uncertainty in the prediction can be attributed to several factors. First, we inverted the bathymetry with the assumption of constant rock density. However, the sedimentary layers are present all over the Arctic. The sediments cover the subseafloor structures that are the main source of gravity. Thus, the correlation between gravity and bathymetry becomes less significant. Second, the remaining long wavelength error from the gravity model may introduce (bias) error to the predicted bathymetry. Third, different scaling factor estimation techniques give different results. The application of robust linear regression techniques is important for the scaling parameter estimations. Last but not least, the linear approximation of the relationship between gravity and topography may not be sufficient at regions with high (seafloor) topographic relief.

The bathymetry predicted from gravity can be combined with the existing bathymetry soundings to make a new hybrid bathymetry of the Arctic, which will be helpful in filling the data gaps between the sparse ship soundings.

Acknowledgments
We thank the NOAA National Centers for Environmental Information (NCEI) for providing IBCAOv3 and the ship soundings available via https://maps.ngdc.noaa.gov/viewers/bathymetry/. This work is partly supported by ESA "CryoSat Plus for Oceans" (CP4O) project. The predicted arctic bathymetry is available via https://ftp.space.dtu.dk/pub/ArcticBATH/.

References

Alvey, A., Gaina, C., Kusznir, N. J., & Torsvik, T. H. (2008). Integrated crustal thickness mapping and plate reconstructions for the high Arctic. *Earth and Planetary Science Letters*, *274*(3-4), 310–321. https://doi.org/10.1016/j.epsl.2008.07.036

Andersen, O. B., & Knudsen, P. (2019). *The DTU17 global marine gravity field—First validation results*, *International Association of Geodesy Symposia*, (). Berlin, Heidelberg: Springer.

Arndt, J. E., Jokat, W., Dorschel, B., Myklebust, R., Dowdeswell, J. A., & Evans, J. (2015). A new bathymetry of the Northeast Greenland continental shelf: Constraints on glacial and other processes. *Geochemistry, Geophysics, Geosystems*, *16*, 3733–3753. https://doi.org/10.1002/2015GC005931

Bamber, J. L., Griggs, J. A., Hurkmans, R. T. W. L., Dowdeswell, J. A., Gogineni, S. P., Howat, I., et al. (2013). A new bed elevation dataset for Greenland. *The Cryosphere*, *7*, 499–510. https://doi.org/10.5194/tc-7-499-2013

Becker, J. J., Sandwell, D. T., Smith, W. H. F., Braud, J., Binder, B., Depner, J., et al. (2009). Global bathymetry and elevation data at 30 arc seconds resolution: SRTM30_PLUS. *Marine Geodesy*, *32*(4), 355–371. https://doi.org/10.1080/01490410903297766

Cancet, M., Andersen, O. B., Lyard, F., Cotton, D., & Benveniste, J. (2018). Arctide2017, a high-resolution regional tidal model in the Arctic Ocean. *Advances in Space Research*, *62*(6), 1324–1343, ISSN 0273-1177. https://doi.org/10.1016/j.asr.2018.01.007

Døssing, A., Hansen, T. M., Olesen, A. V., Hopper, J. R., & Funck, T. (2014). Gravity inversion predicts the nature of the Amundsen Basin and its continental borderlands near Greenland. *Earth and Planetary Science Letters*, *408*, 132–145. https://doi.org/10.1016/j.epsl.2014.10.011

Engen, Ø., Frazer, L. N., Wessel, P., & Faleide, J. I. (2006). Prediction of sediment thickness in the Norwegian–Greenland Sea from gravity inversion. *Journal of Geophysical Research*, *111*, B11403. https://doi.org/10.1029/2005JB003924

Fischler, M. A., & Bolles, R. C. (1981). Random sample consensus: A paradigm for model fitting with applications to image analysis and automated cartography. *Communications of the ACM*, *24*(6), 381–395.

Gardner, J. V., Mayer, L. A., & Armstrong, A. (2006). Mapping supports potential submission to U.N. Law of the Sea. *Eos Transactions American Geophysical Union*, *87*(16), 157–160. https://doi.org/10.1029/2006EO160002

Glebovsky, V. Y., Astafurova, E. G., Chernykh, A. A., Korneva, M. A., Kaminsky, V. D., & Poselov, V. A. (2013). Thickness of the Earth's crust in the deep Arctic Ocean: Results of a 3D gravity modeling. *Russian Geology and Geophysics*, *54*(3), 247–262.

Jakobsson, M., Grantz, A., Kristoffersen, Y., & Macnab, R. (2003). Physiographic provinces of the Arctic Ocean seafloor. *Geological Society of America Bulletin*, *115*(12), 1443–1455.

Jakobsson, M., Mayer, L., Coakley, B., Dowdeswell, J. A., Forbes, S., Fridman, B., et al. (2012). The International Bathymetric Chart of the Arctic Ocean (IBCAO) Version 3.0. *Geophysical Research Letters*, *39*, L12609. https://doi.org/10.1029/2012GL052219

Kenyon, S., & Forsberg, R. (2008). New gravity field for the Arctic. *Eos, Transactions American Geophysical Union*, *89*(32), 289. https://doi.org/10.1029/2008EO320002

Laske, G., & Masters, G. (1997). A global digital map of sediment thickness. *Eos Transactions American Geophysical Union*, *78*, F483.

Le Brocq, A. M., Payne, A. J., & Vieli, A. (2010). An improved Antarctic dataset for high resolution numerical ice sheet models (ALBMAP v1). *Earth System Science Data*, *2*(2), 247–260. https://doi.org/10.5194/essd-2-247-2010

May, S. D., & Grantz, A. (1990). Sediment thickness in the southern Canada Basin. *Marine Geology*, *93*, 331–347.

Mayer, L. A., & Armstrong, A. (2012). US Law of the Sea cruise to map and sample the US Arctic Ocean margin. University of New Hampshire (UNH), Center for Coastal and Ocean Mapping (CCOM)/Joint Hydrographic Center (JHC)

Mayer, L. A., Calder, B., & Mosher, D. C. (2016). US Law of the Sea cruise to map and sample the US Arctic Ocean margin, Healy 1603. Center for Coastal and Ocean Mapping/Joint Hydrographic Center, University of New Hampshire, Durham, NH

Mayer-Gürr, T., Kvas, A., Klinger, B., Rieser, D., Zehentner, N., Pail, R., et al. (2015). The new combined satellite only model GOCO05s. https://doi.org/10.13140/RG.2.1.4688.6807

McKenzie, D., & Bowin, C. (1976). The relationship between bathymetry and gravity in the Atlantic Ocean. *Journal of Geophysical Research*, *81*(11), 1903–1915. https://doi.org/10.1029/JB081i011p01903

Morlighem, M., Williams, C. N., Rignot, E., An, L., Arndt, J. E., Bamber, J. L., et al. (2017). BedMachine v3: Complete bed topography and ocean bathymetry mapping of Greenland from multibeam echo sounding combined with mass conservation. *Geophysical Research Letters*, *44*, 11,051–11,061. https://doi.org/10.1002/2017GL074954

Pail, R., Fecher, T., Barnes, D., Factor, J. F., Holmes, S. A., Gruber, T., & Zingerle, P. (2018). Short note: The experimental geopotential model XGM2016. *Journal of Geodesy*, *92*, 443–451. https://doi.org/10.1007/s00190-017-1070-6

Parker, R. L. (1973). The rapid calculation of potential anomalies. *Geophysical Journal of the Royal Astronomical Society*, *31*, 447–455. https://doi.org/10.1111/j.1365-246X.1973.tb06513.x

Pavlis, N. K., Holmes, S. A., Kenyon, S. C., & Factor, J. K. (2012). The development and evaluation of the Earth Gravitational Model 2008 (EGM2008). *Journal of Geophysical Research*, *117*, B04406. https://doi.org/10.1029/2011JB008916

Schaffer, J., Timmermann, R., Arndt, J. E., Kristensen, S. S., Mayer, C., & Morlighem, M. (2016). A global, high-resolution data set of ice sheet topography, cavity geometry, and ocean bathymetry. *Earth System Science Data*, *8*(2), 543–557.

Smith, W. H. F., & Sandwell, D. T. (1994). Bathymetric prediction from dense satellite altimetry and sparse shipboard bathymetry. *Journal of Geophysical Research*, *99*(B11), 21,803–21,824. https://doi.org/10.1029/94JB00988

Weatherall, P., Marks, K. M., Jakobsson, M., Schmitt, T., Tani, S., Arndt, J. E., et al. (2015). A new digital bathymetric model of the world's oceans. *Earth and Space Science*, *2*, 331–345. https://doi.org/10.1002/2015EA000107

Wessel, P., & Smith, W. H. (1991). Free software helps map and display data. *Eos, Transactions American Geophysical Union*, *72*(41), 441–446.

Wessel, P., Smith, W. H., Scharroo, R., Luis, J., & Wobbe, F. (2013). Generic mapping tools: improved version released. *Eos, Transactions American Geophysical Union*, *94*(45), 409–410.

Wessel, P., & Smith, W. H. F. (1996). A global, self-consistent, hierarchical, high-resolution shoreline database. *Journal of Geophysical Research*, *101*(B4), 8741–8743. https://doi.org/10.1029/96JB00104